Injection strategy - a driver of atmospheric circulation and ozone response to stratospheric aerosol geoengineering

Ewa M. Bednarz[1,2,3], Amy H. Butler[2], Daniele Visioni[3,4], Yan Zhang[3], Ben Kravitz[5,6], Douglas G. MacMartin[3]

1. Cooperative Institute for Research in Environmental Sciences (CIRES), University of Colorado Boulder, Boulder, CO, USA
2. National Oceanic and Atmospheric Administration (NOAA), Chemical Sciences Laboratory (CSL), Boulder, CO, USA
3. Sibley School of Mechanical and Aerospace Engineering, Cornell University, Ithaca, NY, USA
4. National Center for Atmospheric Research (NCAR), Atmospheric Chemistry Observations and Modelling (ACOM), Boulder, CO, USA
5. Department of Earth and Atmospheric Sciences, Indiana University, Bloomington, IN, USA
6. Atmospheric Sciences and Global Change Division, Pacific Northwest National Laboratory, Richland, WA, USA

Correspondence to: Ewa M. Bednarz (ewa.bednarz@noaa.gov)

Abstract.

Despite offsetting global mean surface temperature, various studies demonstrated that Stratospheric Aerosol Injection (SAI) could influence the recovery of stratospheric ozone and have important impacts on stratospheric and tropospheric circulation, thereby potentially playing an important role in modulating regional and seasonal climate variability. However, so far most of the assessments of such an approach have come from climate model simulations in which SO_2 is injected only in a single location or a set of locations.

Here we use CESM2-WACCM6 SAI simulations under a comprehensive set of SAI strategies achieving the same global mean surface temperature with different locations and/or timing of injections: an equatorial injection, an annual injection of equal amounts of SO_2 at 15°N and 15°S, an annual injection of equal amounts of SO_2 at 30°N and 30°S, and a polar strategy injecting SO_2 at 60°N and 60°S only in spring in each hemisphere.

We demonstrate that despite achieving the same global mean surface temperature, the different strategies result in contrastingly different magnitudes of the aerosol-induced lower stratospheric warming, stratospheric moistening, strengthening of stratospheric polar jets in both hemispheres and changes in the speed of the residual circulation. In conjunction with the differences in direct radiative impacts at the surface, these drive different impacts on the extratropical modes of variability (Northern and Southern Annular Mode), including important consequences on the northern winter surface climate, as well as on the intensity of tropical tropospheric Walker and Hadley Circulations, which drive tropical precipitation patterns. Finally, we demonstrate that the choice of injection strategy also plays a first-order role in the future evolution of stratospheric ozone under SAI throughout the globe. Overall, our results contribute to an increased understanding of the fine interplay of various

35   radiative, dynamical and chemical processes driving the atmospheric response to SAI, as well as lay the ground for designing
an optimal SAI strategy that could form a basis of future multi-model intercomparisons.

1. Introduction

Stratospheric Aerosol Injection (SAI) is a proposed solar geoengineering method aimed at temporarily offsetting some of the
negative impacts of rising greenhouse gas levels and the resulting increases in surface temperatures. The method would involve
40   the injection of sulfate aerosols or their precursors into the lower stratosphere, which would then reflect a portion of the
incoming solar radiation in a manner similar to that observed during past explosive volcanic eruptions (e.g. Kravitz and
MacMartin, 2020).

Many SAI studies focus primarily on the direct impacts of SAI caused by the reduction in the incoming solar radiation on the
45   large-scale temperature or precipitation pattern. However, SAI would not perfectly cancel the GHG-induced temperature
changes because the spatial and temporal pattern of the long-wave radiative forcing from GHGs is very different from that of
the reflection of solar radiation by aerosols (e.g. Bala et al., 2008). In addition, the absorption of radiation by stratospheric
sulfate will increase temperatures in the lower stratosphere. Both effects can drive important dynamical changes in
stratospheric and tropospheric circulation, resulting in potential 'side-effects' on a regional and/or seasonal scale. These
50   include impacts on extratropical modes of variability, namely the Northern Annular Mode (NAM) and North Atlantic
Oscillation (NAO) in the Northern Hemisphere (NH) (e.g. Banerjee et al., 2021, Jones et al., 2022), and Southern Annular
Mode (SAM) in the Southern Hemisphere (SH) (e.g. Bednarz et al., 2022a, 2022b). Both of these are tightly coupled to the
variability in the winter stratosphere (Thompson and Wallace, 1998, 2000; Baldwin and Dunkerton, 2002), and forced changes
in circulation often project onto these modes (e.g. Thompson et al., 2000; Ring and Plumb, 2007). SAI can also drive changes
55   in the tropical tropospheric circulation, including the Hadley Circulation (e.g. Cheng et al., 2021) and Walker Circulation (e.g.
Simpson et al., 2019), which drive precipitation patterns over large parts of the tropical and subtropical regions.

SAI-induced changes in stratospheric composition can also be important. First, stratospheric concentrations of water vapour
are primarily driven by the tropical cold point tropopause temperatures as any excess water vapour is dehydrated upon entry
60   into the stratosphere. The SAI-induced increase in lower stratospheric temperatures due to aerosol heating would increase cold
point tropopause temperatures and thus allows more water vapour to enter the stratosphere (e.g. Krishnamohan et al., 2019;
Visioni et al., 2021a; Bednarz et al., 2023). In the lower stratosphere, water vapour acts as a greenhouse gas, trapping a portion
of outgoing terrestrial radiation and reradiating it back to the surface. This effect has been shown to constitute an important
contribution to the man-made climate warming (Forster and Shine, 1999; Solomon et al., 2010), although few studies have
65   estimated the importance of this effect under SAI. Based on three out of four models participating in the GeoMIP G4
experiment, the radiative forcing of aerosol-induced increase in stratospheric water vapour – 0.02-0.35 ppmv at 100 hPa in the

tropics - was estimated at 0.004-0.077 Wm^{-2} (Pitari et al., 2014), but estimates under different SAI scenarios and strategies or in more models have so far been missing. Second, SAI will also impact the stratospheric ozone layer via multiple mechanisms, such as an enhancement of heterogeneous halogen activation on sulfate aerosols, and the resulting halogen catalysed chemical

70 ozone loss, as well as via the SAI-induced changes in the large-scale stratospheric transport (e.g. Tilmes et al., 2018a; 2021; 2022). Stratospheric ozone plays an important role in ecosystem and human health by shielding the surface from harmful UV-B radiation, and so its past and future evolution has been subject to thorough attention due to international accords such as the Montreal Protocol and its subsequent amendments and adjustments. Recently, the impacts of SAI on ozone were addressed in a new chapter of the WMO Ozone Assessment report (WMO, 2022).

75

Importantly, by far most of the assessment of climate impacts from a hypothetical SAI deployment comes from simulations that inject SO$_2$ only at a single location, usually at or near the equator (e.g. as it was done in most of the GeoMIP experiments, e.g. Kravitz et al., 2015; Visioni et al., 2021b), or a combination of locations (e.g. 30°N + 15°N + 15°S + 30°S injections, as was done in the recent GLENS and ARISE-SAI CESM simulations, Tilmes et al., 2018b; Richter et al., 2022). Some

80 assessment of the injection latitude dependence for the simulated climate impacts comes from simulations injecting fixed amounts of SO$_2$ at single latitudes (Richter et al., 2017; Tilmes et al., 2018a; Bednarz et al., 2023; Visioni et al., 2023), and these demonstrate a strong dependence of the simulated atmospheric and surface climate impacts on the latitude of SAI. However, whilst important for understanding mechanisms driving the SAI response, such single-point SAI simulations are unlikely to be representative of a plausible SAI deployment strategy as single hemispheric deployments would strongly impact

85 interhemispheric temperature gradients and, thus, lead to substantial precipitation changes (e.g. Haywood et al., 2013; Visioni et al., 2023). Recently, Zhang et al. (2023) introduced a set of comprehensive SAI strategies, simulated in the Community Earth System Model (CESM2-WACCM6), achieving the same global mean surface temperature through different combinations of location and timing of the SO$_2$ injections. These included an annual equatorial injection, an annual injection of equal amounts of SO$_2$ at 15°N and 15°S, an annual injection of equal amounts of SO$_2$ at 30°N and 30°S, and a polar strategy

90 injecting SO$_2$ at 60°N and 60°S only in spring in each hemisphere. The study demonstrated that despite achieving the same global mean surface temperatures, the different injection strategies can lead to different impacts on regional surface climate. Here we extend the analysis of Zhang et al. (2023) to include the SAI impacts on stratospheric climate and chemistry, including changes in water vapour and ozone, and on atmospheric circulation. The latter includes impacts on the stratospheric Brewer Dobson Circulation and modes of extratropical variability, with resulting impacts on the mid-/high latitude surface climate,

95 and on Hadley and Walker Circulations, which drive regional tropical precipitation patterns.

2. Methods

2.1 SAI strategies and model simulations

We use the CESM2-WACCM6 Earth system model (Gettelman et al., 2019; Danabasoglu et al., 2020) with interactive ocean and sea-ice, interactive modal aerosol microphysics (MAM4, Liu et al., 2016), interactive middle atmosphere chemistry (MA, Davis et al., 2023) and internally generated Quasi-Biennial Oscillation. The horizontal resolution is 1.25° longitude by 0.9° latitude, with 70 vertical levels in hybrid-pressure coordinate up to ~140 km.

We use the set of SAI simulations introduced by Zhang et al. (2023). The Coupled Model Intercomparison Project Phase 6 (CMIP6) Shared Socioeconomic Pathway SSP2-4.5 experiment is chosen as the background emission scenario. Four SAI strategies are used, covering the period 2035 to 2069 inclusive. These employ a feedback algorithm that adjusts SO_2 injection rates in order to maintain the global mean surface temperatures at the baseline level, corresponding to 1.0°C above preindustrial conditions (henceforth referred to as BASE_1.0) and in CESM2 historical and SSP2-4.5 runs corresponds to the mean over the period 2008-2027 (see MacMartin et al. 2022, for details on the definition of climate targets).

The first strategy, henceforth denoted 'EQ', injects SO_2 at the equator at 22 km at a constant rate throughout a year. In the second and third strategy, denoted '15N+15S' and '30N+30S', SO_2 is injected at 22 km at a constant rate throughout a year and at equal rates at a pair of injection latitudes - 15°N and 15°S or 30°N and 30°S, respectively. The fourth strategy, denoted 'POLAR', injects SO_2 at 15 km with equal rates at both 60°N and 60°S but only during spring at each hemisphere (so MAM for 60°N and SON for 60°S). Averaged over the last 20-years of the simulations, the injection rates needed to maintain the global mean near-surface air temperatures at 1.0C above preindustrial levels are 21.0, 16.3, 14.4 and 20.4 Tg-SO_2/yr for EQ, 15+15, 30+30 and POLAR, respectively (Zhang et al. 2023). In all cases, we analyse the last 20-years of the simulations - i.e. 2050-2069 - and, with the exception of the results in Section 6, compare them to their baseline period - i.e. 2008-2027.

2.2. The simulated sulfate aerosol fields

The characteristics of the stratospheric circulation imply that the overall distribution of sulfate aerosols strongly depends on the location of the injection. In particular, the equatorial 'EQ' strategy and, to a lesser extent, the tropical '15N+15S' strategy lead to significant confinement of aerosols inside the tropical pipe and thus, to the largest aerosol mass mixing ratios at low latitudes (Fig. S1, top). The subtropical '30N+30S' strategy, where SO_2 is injected largely outside the tropical pipe, allow for more transport of aerosols to the mid- and high latitudes, leading to more uniform aerosol distribution. Finally, the 60°N and 60°S injections in POLAR result in the highest aerosol concentrations simulated in the high latitudes, with only very small levels in the tropics. Notably, the lifetime of aerosols decreases as SO_2 is injected away from the equator and into the mid- and high latitudes (Visioni et al., 2023), leading to smaller average sizes of sulfate aerosols (see Fig. 4b in Zhang et al., 2023). In

POLAR, this manifests as the smallest sulfate mass mixing ratios (Fig. S1, top) but the largest sulfate surface area densities (Fig. S1, middle) simulated in the stratosphere compared to the other strategies.

130   Since stratospheric circulation varies seasonally, the simulated aerosol fields under annual injections (EQ, 15N+15S, and 30N+30S) also exhibit a seasonal cycle in their optical depths (Fig. S1, bottom). These changes are, however, much smaller than the seasonal cycle in aerosol optical depths simulated in POLAR, where SO_2 is injected only in spring at each hemisphere. The ~1 month timescale for SO_2-to-aerosol conversion leads to the largest concentrations of sulfate in POLAR simulated in the summer in each hemisphere, before the aerosols are rapidly removed over the following season (see also Lee et al. 2021).

135   **3. Annual mean changes in stratospheric climate**

3.1 Temperatures

Figure 1 (top) shows the yearly mean changes in atmospheric temperatures simulated across the different strategies compared to the baseline period. In particular, Fig.1 (left, middle) shows the vertical cross-sections of the responses in EQ and POLAR (which correspond to two extreme ends of our potential strategy space, see Section 2.2), with the analogous responses in
140   15N+15S and 30N+30S shown in Supplementary Material (Fig. S2, top). The right panel in Fig. 1 (top) shows the changes simulated in each of the four strategies in the tropical lower stratosphere (20°S-20°N, 50 hPa).

We find a strong dependency of the magnitude of the tropical lower stratospheric heating on the SAI strategy, with EQ showing the strongest warming of ~8.8 K at 50 hPa (20°S-20°N) and POLAR showing the smallest warming of ~0.4 K in that region.
145   This can be explained simply by the spatial distribution of the simulated aerosol cloud, and the amount of sulfate in the tropical lower stratosphere (Section 2, Fig. S1). The results also indicate some strategy dependence of the poleward extent of the lower stratospheric warming, although this is more difficult to isolate as the extratropical stratospheric temperature responses are also strongly controlled by dynamical processes.

3.2 Water vapour

150   The magnitude of the SAI-induced tropical lower stratospheric warming controls cold point tropopause temperatures and is thus directly related to the associated changes in stratospheric water vapour. As shown in the bottom panels of Fig. 1, all SAI strategies increase concentrations of water vapour in the stratosphere, with the magnitude of this stratospheric moistening generally tracking the magnitude of the lower stratospheric warming and, thus, SAI strategy. As water vapour in the lower stratosphere acts as a greenhouse gas to warm the troposphere, this secondary effect thus offsets some of the direct tropospheric
155   cooling from the reflection of solar radiation by sulfate aerosols. The particularly strong increase in lower stratospheric water vapour in EQ, up to 75% at 70 hPa, thus constitutes one of the reasons behind particularly low efficacy of this strategy, as discussed in more detail in Zhang et al. (2023). The relative similarity of water vapor response between 30N+30S and POLAR,

despite larger differences in tropical stratospheric temperatures, points to the role of seasonality of the SAI-induced lower stratospheric temperature response for the resulting stratospheric moistening.

160

Regarding the corresponding radiative forcing (RF) from stratospheric moistening, an increase in 1 ppm stratospheric water vapour has been estimated to contribute a radiative forcing of 0.24-0.29 W/m^2 at the tropopause (Forster and Shine, 1999; Solomon et al., 2010). We can estimate the radiative forcing from the SAI-induced stratospheric moistening using the simulated changes in water vapour at 100 hPa, i.e. near the cold point tropopause and where radiative effects of stratospheric water vapour on surface temperatures are particularly strong (e.g. Riese et al., 2012), and assuming a RF of 0.25 W/m^2 per 1 ppm H_2O increase. This gives a RF of 0.54 W/m^2 in EQ (2.2 ppm increase in H_2O at 100 hPa), 0.31 W/m^2 in 15N+15S (1.2 ppm H_2O increase), 0.16 W/m^2 in 30N+30S (0.7 ppm H_2O increase) and 0.15 W/m^2 in POLAR (0.6 ppm H_2O increase). This can be compared with the RF of GHGs that is being offset, which for the SSP2-4.5 scenario equates to 1.42 W/m^2 difference between 2050-2069 and 2008-2027 (Fricko et al., 2017), or with the RF of sulfate itself. For the latter, using the of the top-of-the-atmosphere (TOA) calculations of RF from sulfate from Visioni et al. (2022), whereby a change of 0.588 AOD over 2090-2099 equated to -7.30 W/m^2 at TOA, and the global and annual mean sAOD changes in Fig. S1(bottom) here, we can estimate the TOA RF of sulfate in these experiments ranging from -2.90 W/m^2 in EQ to -1.43 W/m^2 in POLAR. Hence, whilst the RF from the SAI-induced stratospheric moistening is much smaller than the direct RF of sulfate, it is nonetheless an important contributor and varies strongly across the different strategies; it thus needs to be factored in any considerations of efficacies of individual strategies.

3.3. Stratospheric large-scale circulation

3.3.1 Zonal winds

Figure 2 (top) shows the associated changes in yearly mean zonal winds. SAI-induced warming in the tropical lower stratosphere increases equator-to-pole meridional temperature gradients near the tropopause and lower stratosphere and, thus, forces strengthening of stratospheric jets in both hemispheres. The westerly response is generally found throughout the year for the annual injection strategies, and more intermittently for the seasonal injection in POLAR (Fig. S4). In accord with the strong dependence of the magnitude of the lower stratospheric warming on the SAI strategy (Fig. 1, top), as well as its poleward extent, we also find a strong strategy dependence of the magnitude of the resulting polar vortex strengthening, with EQ showing the strongest westerly responses in both hemispheres and POLAR the smallest (e.g. 7 ms^{-1} and 1 ms^{-1} at 50°S and 30 hPa for EQ and POLAR, respectively). For POLAR, the smallest magnitude of the NH stratospheric polar jet strengthening is also partially caused by the increased tropospheric source of wave activity in that strategy, as illustrated by increased poleward meridional heat flux (V'TH') in the northern midlatitude troposphere (Fig. 2, bottom). An increased vertical flux of tropospheric wave activity into the stratosphere could be driven by the overcompensation of Arctic sea-ice extent in POLAR compared to the baseline period (Fig. S5; see also Zhang et al., 2023). Changes in Arctic sea-ice can drive important changes

190   in wave propagation into the stratosphere and thus vortex strength and temperature (Scinocca et al., 2009; Sun et al., 2014; England et al., 2018); here this effect can thus contribute to the smallest magnitude of the northern polar vortex strengthening in POLAR.

Interestingly, in all four strategies the SAI-induced strengthening of the SH polar vortex is larger than in the NH (e.g. 7 ms^{-1}

195   in the SH and 3 ms^{-1} in the NH at 50 hPa for EQ). This could be because of the associated reduction in poleward heat flux simulated in the SH across the three strategies injecting SO_2 in the tropics/subtropics, i.e. EQ, 15+15, 30+30 (Fig. 2, bottom). The SAI-induced reduction in tropospheric wave flux propagating into the stratosphere helps to strengthen stratospheric winds in the SH, thereby amplifying the initial thermal wind response driven by the enhanced meridional temperature gradients in the lower stratosphere. Accordingly, a smaller magnitude of the SH westerly response is found during summer (Fig. S4), when

200   the response largely reflects just the thermal wind response as planetary waves can't propagate when background winds are easterly. The reduction of tropospheric wave source in the SH in these three strategies could be because of the associated reduction in the meridional temperature gradients in the southern hemisphere troposphere (Fig. 1 and Fig. S2).

3.3.2. Brewer Dobson Circulation

The SAI-induced warming in the tropical lower stratosphere can also drive changes in the strength of the large-scale residual

205   circulation. Figure 3 shows the associated changes in Transformed Eulerian Mean vertical and meridional velocities. The increase in static stability of the troposphere as the result of lower stratospheric warming weakens the upwelling in the upper troposphere and lowermost stratosphere (UTLS) region (Fig. 3, top), also sometimes referred to as the shallow branch of the Brewer Dobson Circulation (BDC), e.g.: Abalos et al. (2021). By mass continuity, the reduction in vertical velocities is associated with reductions in meridional velocities at the same levels (Fig. 3, bottom). In agreement with the strong dependence

210   of the magnitude of lower stratospheric warming on the SAI strategy (Section 3.1.), we find a strong correlation between the magnitude of the SAI-induced weakening of the circulation in that region (Fig. 3, right), with the largest changes in EQ and smallest in POLAR.

Warming in the lower stratosphere also reduces the stability of the stratosphere itself, thereby accelerating the deep branch of

215   the BDC. As with the shallow branch, we find a strong dependence of the magnitude of the response on the SAI strategy. However, there are now more spatial differences in the responses across strategies (Fig. S6), with the upwelling increasing mainly near the latitude of injection. In general, SAI-induced changes in residual circulation in both its shallow and deep branches will drive important changes in stratospheric transport of chemical species, including ozone (Section 6) and water vapour (Section 3.2), thereby modulating their distributions. It will also feedback on the simulated distributions of sulfate itself

220   (e.g. Visioni et al., 2020).

4. Seasonal changes in the high latitude circulation and climate

4.1 Northern Hemisphere

Changes in the strength of the stratospheric polar vortex can propagate down to the troposphere, affecting the distribution of sea-level pressure and latitudinal shifts of the eddy-driven tropospheric jets. In the NH, this coupling plays an important role in determining winter temperature and precipitation patterns across the mid- and high latitudes (Thomson and Wallace, 1998). Figure 4 shows the DJF changes in sea-level pressure (top), zonal winds at 850 hPa (middle) and near-surface air temperatures (bottom) simulated in the NH in the different SAI strategies. The NAO sea-level pressure index is calculated as the difference in sea-level pressure in the Atlantic sector between the midlatitudes (280°E-360°E, 30°N-60°N) and the polar cap (70°N-90°N, all longitudes). The Pacific sea-level pressure index is defined as the sea-level pressure in the Aleutian low region (140°E-240°E, 30°N-70°N). The position of the eddy driven jet is defined as the latitude of the maximum zonal wind at 850 hPa; this is done separately for the Atlantic (280°E-360°E) and Pacific (140°E-240°E) sectors. Finally, near-surface air temperatures over Eurasia and Alaska are defined as the average over 50°N-85°N, 20°E-120°E and over 45°N-70°N, 180°E-240°E, respectively.

4.1.1. Atlantic sector

We find that the SAI-induced strengthening of the stratospheric polar vortex (Fig. 2) only propagates down to the surface and leads to a clear NAO-like signature for EQ and 15N+15S (Fig. 4, top). The positive NAO response in these strategies is associated with a poleward shift of the eddy-driven jet in the Atlantic sector (Fig. 4, middle), as well as a significant warming in the northern Eurasian region (Fig. 4, bottom). A small cooling also occurs in these SAI strategies in western Europe (Fig. S8, left panel). In contrast, no clear NAO-signature or jet shift is found over the Atlantic sector for 30N+30S and POLAR, with the 30N+30S showing only a suggestion of a small equatorward shift of the North Atlantic jet stream instead. We note that all 4 strategies show a poleward jet shift near the jet exit region over Europe (right panel in Fig. S7), and that response is opposite sign to the changes occurring over the jet entrance region in the west Atlantic sector under 30S+30N and POLAR.

The lack of strong changes in sea level pressure or tropospheric jet shift over the Atlantic sector in POLAR is consistent with the absence of any substantial strengthening of the NH stratospheric polar vortex (Fig. 2). Despite that, the POLAR strategy does show a marked cooling in the northern Eurasian region, as well as more broadly across much of the Arctic. We hypothesize that this cooling is a manifestation of the radiative effects from the overcompensation of Arctic sea-ice in that strategy compared to the baseline period (Fig. S5; also Zhang et al. 2023). Increased sea ice would lead to higher surface albedo and greater longwave cooling of the polar surface (e.g. Lee et al., 2023). Changes in sea-ice are also known to strongly impact tropospheric wave source in the NH (e.g. Scinocca et al., 2009; Sun et al., 2014). Thus, as discussed in Section 3, this overcompensation of sea-ice in POLAR also enhances the flux of tropospheric wave activity (Fig. 2, bottom), which may

8

weaken the already weakest stratospheric westerly wind response in that strategy expected from the thermal wind considerations alone (Fig. 2, top).

4.1.2. Pacific sector

255 In the Pacific sector, EQ, 15N+15S and 30N+30S all show weakening of the sea-level pressure over the north Pacific (Fig. 4, top) – corresponding to the strengthening of the Aleutian low – as well as an equatorward shift of the winter jet in that region (Fig 4, middle). The weakening of the Pacific sea-level pressure increases in magnitude and moves slightly poleward as the aerosol precursors are injected away from the equator and more in the subtropics (see. Fig. S7). The SAI-induced strengthening of the Aleutian low gives rise to stronger northerly advection of tropical air on the eastern flank of the anomalous low,

260 increasing temperatures over the western US and Alaskan region (Fig. 4, bottom). Stronger northerly advection in the eastern Pacific also brings in more moist air, and the stronger southerly advection in the western Pacific brings in more dry air; although we note that in these simulations the resulting statistically significant precipitation changes are located mainly above the ocean regions (Fig. S9). Unlike the dynamically-driven top-down response from the stratosphere in the Atlantic sector, the Pacific response is likely driven directly in the troposphere. Strengthening of the Aleutian low, typically accompanied also by

265 anomalously higher pressures over Canada and anomalously low pressures over the southeast US, is suggestive of a large-scale planetary wave response, typical of wave trains forced by changes to tropical Pacific convective heating (See Section 5). The Pacific-North American sea-level pressure response is thus likely indicative of large-scale teleconnections from the SAI response in the tropical troposphere. As in the Atlantic sector, POLAR does not show strong changes in sea level pressure or jet shift over the Pacific sector.

270 4.2. Southern Hemisphere

The propagation of stratospheric wind anomalies down to the surface is also an important driver of year-to-year climate variability in the SH, but unlike in the NH where the stratosphere-troposphere coupling occurs primarily in winter, this coupling generally maximizes in austral spring and summer. Figure 5 shows DJF changes in sea-level pressures (top) and zonal wind at 850 hPa (bottom) simulated in the SH in the different strategies. We find that both the EQ and POLAR strategies show pattern

275 of sea-level pressure consisting of increased pressure in the mid-latitudes and decreased pressure over the Antarctic. This corresponds to the positive phase of Southern Annular Mode (SAM; here defined as the difference in zonal mean sea-level pressure between 50°S and 70°S), and is accompanied by a statistically significant poleward shift of the SH eddy-driven jet. The magnitudes of these responses are very similar between the EQ and POLAR strategies.

280 Interestingly, the magnitude of these responses decreases under 15N+15S relative to EQ and POLAR, and the response changes sign under 30N+30S which shows a negative phase of SAM and a small equatorward shift of eddy-driven jet instead. Bednarz et al. (2022b) analysed the SAM changes under fixed single point SO_2 injections imposed between 30°S and 30°N in the same CESM2 version, and showed that the SAM response becomes negative under SO_2 injections in the SH as the injections are

moved further into the subtropics. That work suggested that this occurs because of the poleward extent of lower stratospheric

285 heating impacting planetary wave propagation in the stratosphere as well as eddy heat and momentum fluxes in the troposphere below. It is thus plausible that the SAM and jet responses in the EQ, 15N+15S and 30N+30S strategies here are largely dynamically driven by the lower stratospheric heating, in a manner consistent with the mechanisms suggested in Bednarz et al. (2022b). The SH high latitude responses in POLAR on the other hand, where the SAI direct impact is largely focused in the mid- and high latitudes in austral summer (Fig. S1, bottom), is likely primarily radiatively driven by the direct cooling of

290 Antarctic surface temperatures caused by the reduced summer insolation under SAI, thereby forcing changes in tropospheric winds and sea level pressures. However, specially designed simulations would be needed to fully diagnose such a mechanism.

We note that an qualitatively and quantitatively similar results regarding the overall behaviour of the SAM and SH eddy-driven jet are obtained if annual mean changes are examined instead of the austral summer responses (right panels in Fig. 5).

295 **5. Impacts on tropical tropospheric circulation**

While changes in global mean precipitation are expected to scale largely, albeit not fully, with the corresponding changes in global mean temperatures (Niemeier et al., 2013; Zhang et al., 2023), any regional SAI-induced precipitation responses will be in part related to changes in the intensity and position of large-scale tropospheric circulation patterns, including the tropical Hadley and Walker Circulations.

300

Figure 6 shows the simulated yearly mean changes in (middle) meridional and (bottom) zonal mass stream function. Shown also in the top panels are the corresponding changes in yearly mean precipitation under EQ and POLAR for reference. As it was done for instance in Guo et al. (2018), we define meridional and zonal mass stream functions (ψ_m and ψ_z) according to Eq. (1) and (2), respectively:

305

$$\varphi_m = \frac{2\pi a \cos(\phi)}{g} \int_0^p V \, dp \quad (Eq.1)$$

$$\varphi_z = \frac{2\pi a}{g} \int_0^p U_D \, dp \quad (Eq.2)$$

where a is Earth radius, g is the gravitational acceleration, φ is latitude, V is meridional wind, and U_D is the divergent

310 component of zonal wind averaged between 10°S-10°N.

We use four metrics of tropospheric circulation. The intensity of the Hadley Circulation is calculated as the difference in ψ_m at 500 hPa between the northern (10°N-25°N) and southern (25°S-0°) cells. The intensity of the Walker Circulation is

calculated similarly but using the difference in ψ_z at 400 hPa between the Pacific (180°E-240°E) and Indian Ocean (60°E-

315   120°E) cells. The position of the Intertropical Convergence Zone (ITCZ) is defined as the latitude near the equator where ψ_m

at 500 hPa changes sign. The position of the upwelling branch of the Walker Circulation, i.e. the transition between its Pacific

and Indian Ocean cells, is defined as the longitude between 80°E-200°E where ψ_z at 400 hPa changes sign.

We note that a different commonly used metric of the intensity of Walker Circulation used in the literature (e.g. Kang et. al.

320   2020) is the difference in sea-level pressure between the East Pacific (160°W to 80°W, 5°S to 5°N) and the Indian Ocean/west

Pacific (80°E to 160°E, 5°S to 5°N) regions. Since the use of this metric leads to slightly different results we also include this

metric in Fig. 6 (circles and dashed lines).

5.1. Intensity changes

We find a strong strategy dependence of the simulated changes in the intensity of the Hadley and Walker Circulations. For the

325   Hadley Circulation, EQ shows the largest weakening of the Hadley Circulation, followed by 15N+15S. In contrast, the two

other strategies - 30N+30S and POLAR – do not show significant changes in the Hadley Circulation strength in the annual

mean. For the Walker Circulation, weakening of its intensity is simulated under all 4 SAI strategies, with larger responses

found for the tropical and subtropical injections (EQ, 15N+15S and 30N+30S) and the weakest response in POLAR. The

stronger weakening in EQ and 15N+15S coincides with stronger near-air surface temperature decreases over the Maritime

330   Continent and increases over the eastern Pacific (Fig. S12) indicative of a canonical El-Nino like response; this in turn

coincides with more strongly suppressed convection over the western Pacific basin and relatively enhanced convection over

the eastern Pacific Ocean (Fig. 6, top, Fig. S11, top). In POLAR, near-surface air temperatures increase more broadly over the

equatorial Pacific (Fig. S12) with weaker enhancement of convective precipitation over eastern Pacific (Fig. 6, top), suggestive

of more central Pacific type El-Nino like response (e.g. Yeh et al., 2009). We note that increased convective precipitation in

335   the different El Nino regions can drive different teleconnections patterns (e.g. Calvo et al., 2017), and this effect likely

contributes to the strengthening of the Aleutian low simulated in the Northern Pacific under EQ, 15N+15S and 30N+30S in

boreal winter (Section 4.1.2).

In general, a weakening of tropospheric Hadley and Walker Circulations corresponds to a weakening of the climatological

340   precipitation patterns, such that the regions characterised by climatologically high precipitation receive anomalously less

precipitation, and the regions characterised by the climatologically lower precipitation receive anomalously more precipitation

(i.e. dry gets wetter and wet gets drier). The results show that the tropical tropospheric circulation weakens most under

strategies injecting SO_2 in the tropics and least under high latitude strategy. This behaviour likely arises because of the

combination of how much cooling occurs in each strategy in the tropical troposphere (compared to higher latitudes) as well as

345   to the strength and meridional extent of lower stratospheric heating. The latter increases tropospheric static stability and thus

reduces tropical convection, thus adding on to the decrease in the intensity brought about by the purely thermodynamic considerations. See Zhang et al. (2023) for further discussion.

5.2. Position changes

In contrast to the strong strategy dependence of the SAI impacts on the intensity of tropical tropospheric circulation, little
350   strategy dependence is found for the changes in the position of the Hadley and Walker Circulations. All SAI strategies show a southward shift of the ITCZ (as also shown in Zhang et al., 2023) as well as an eastward shift of the Walker Circulation. These changes are likely related to the corresponding GHG-induced changes in these metrics under the control SSP2-4.5 scenario (grey points in Fig. 6, right column) and their imperfect compensation under SAI in general. An exception is a stronger eastward shift of the Walker Circulation under 30N+30S compared to the other strategies; this drives a significant decrease in
355   precipitation over the Maritime Continent and Australia, and increased precipitation over a large part of the equatorial Pacific (Fig. S11). The stronger eastward shift of the Walker Circulation in 30N+30S also corresponds to larger weakening of its intensity as measured by the sea-level pressure method (points and dashed lines in the bottom right panel in Fig. 6). The stronger response of the Walker Circulation position under 30N+30S compared to other strategies may not be robust (the error bars overlap); regardless, the causes for these different responses are not yet fully understood and remain to be explored.

360   ## 6. Impacts on stratospheric ozone

Figure 7 shows the annual mean changes in ozone mixing ratios and total ozone columns for each of the four injection strategies. In this case we use a comparison against the control SSP2-4.5 simulation during the same period (2050-2069), as opposed to a past period with similar global mean surface temperatures as was done in other sections; this avoids complications from the concurrent long-term changes in ozone caused by long-term changes in ozone depleting substances and greenhouse
365   gases. This approach allows for a better isolation of the impact from increased stratospheric sulfate aerosol load.

6.1. Tropics

The increase in lower stratospheric temperatures (Section 3.1) and the resulting weakening of upwelling in the upper troposphere and lower stratosphere (Section 3.3.2) increases ozone concentrations in the tropical lower stratosphere as less ozone poor air is transported from the troposphere. We find a strong strategy dependence of the magnitude of this ozone
370   response, in line with the strong strategy dependence of the SAI-induced changes in lower stratospheric temperatures and transport. A strong correlation between SAI-induced impacts on lower stratospheric temperatures, ozone and transport was also previously reported from other studies, e.g. Bednarz et al. (2023), Tilmes et al. (2022). SAI-induced changes in ozone in the middle stratosphere are, in turn, a function of the SAI-induced strengthening of the deep part of the BDC (Fig. 3) and, thus, also depend on the SAI strategy, with largest changes for EQ and very small changes for POLAR. As a result of these different
375   factors, when integrated over the depth of the atmosphere, EQ shows an SAI-induced total column ozone loss of ~10 DU near

the equator (as the ozone decrease at ~30 hPa outweighs the ozone increase below), while no significant tropical total column ozone changes are simulated under the other SAI strategies in the yearly mean.

6.2. Northern Hemisphere

The EQ and 15N+15S strategies increase total column ozone in the NH mid and high latitudes throughout the year (Fig. 7-8)
380 - 18 DU and 8 DU on average between 30°N-90°N in yearly mean for EQ and 15N+15S, respectively - because of the SAI-induced changes in ozone transport (Section 3.3.2). In the mid- and upper stratosphere, the acceleration of the BDC brings more ozone from its photochemical production region (i.e. tropical mid-stratosphere) to higher latitudes. In the lower stratosphere, the SAI-induced weakening of the shallow branch of the BDC also increases extratropical ozone levels as less ozone-poor air is brought from the tropical lower stratosphere.

385 In contrast, 30N+30S and POLAR show no strong yearly mean total column ozone changes in the NH mid and high latitudes. This occurs because the dynamically-driven ozone increases are much smaller (as the lower stratospheric warming and the resulting BDC changes are weaker) and these are generally offset by the ozone decreases in the lowermost stratosphere due to the enhanced heterogeneous halogen activation on sulfate (as more aerosols are now found in the mid and high latitudes). The chemical losses can however dominate during parts of the year, leading to small ozone reductions (up to ~10 DU) at mid and
390 higher latitudes in the NH spring (30N+30S) and summer (30N+30S and POLAR), Fig. 8.

6.3. Southern Hemisphere

In the SH, SAI-induced ozone changes in the mid and high latitudes are even more complex and reflect competing impacts from (i) enhanced heterogenous halogen activation on sulfate and thus chemical ozone loss (strongest for 30N+30S and POLAR), (ii) dynamically driven ozone reductions inside the Antarctic polar vortex as stratospheric winds strengthen under
395 the tropical lower stratospheric warming (strongest in EQ and 15N+15S), and (iii) enhanced transport of ozone-rich air in the middle stratosphere under the SAI-induced acceleration of the deep branch of BDC, and reduced transport of ozone-poor air in the lowermost stratosphere under the SAI-induced deceleration of the shallow BDC branch (strongest in EQ and 15N+15S).

Thus, in the SH subtropics ozone columns increase under EQ and 15N+15S but decrease slightly or stay roughly unchanged
400 for 30N+30S and POLAR. In the mid and high latitudes, all four SAI strategies show significant annual mean column ozone decreases (13 DU, 14 DU, 22 DU and 18 DU ozone loss over 65S-90S for EQ, 15N+15S, 30N+30S and POLAR, respectively, Fig. 7), albeit with differences in magnitudes of these losses between the strategies in different seasons (Fig. 8). While the contribution of halogen catalysed chemical ozone loss from the halogen activation on sulfate is strongest for the 30N+30S and POLAR strategies, the two tropical injections - EQ and 15N+15S - also show significant Antarctic ozone losses in the
405 lowermost stratosphere over large parts of the year, and these are likely dominated by the dynamically-driven reductions in in-mixing of the ozone-rich midlatitude air under stronger stratospheric polar vortex.

The results thus highlight the complex interplay of various processes driving the stratospheric ozone response to SAI, and call for more research done in narrowing the associated uncertainties, in particular in a multi-model framework.

7. Summary and discussion

Most of the assessment of atmospheric and climate response from a hypothetical Stratospheric Aerosol Injection to date comes from climate model simulations in which SO_2 is injected only in a single location or a set of locations. Here we use CESM2-WACCM6 SAI simulations under a comprehensive set of SAI strategies introduced by Zhang et al. (2023) that achieve the same global mean surface temperature with different locations and/or timing of injections: an equatorial injection, an annual injection of equal amounts of SO_2 at 15°N and 15°S, an annual injection of equal amounts of SO_2 at 30°N and 30°S, and a polar strategy injecting SO_2 at 60°N and 60°S only in spring in each hemisphere. Building on the initial results in Zhang et al. (2023), we demonstrate that despite achieving the same global mean surface temperature, the different strategies result in contrastingly different impacts on stratospheric temperatures, water vapour, ozone and the large scale stratospheric and tropospheric circulation, with important implications for the surface climate.

First, the absorption of a portion of outgoing terrestrial and incoming solar radiation by sulfate increases temperatures in the tropical lower stratosphere. A strong SAI strategy dependence is found for the magnitude of this warming, ranging from 8.8 K at 50 hPa in the equatorial to 0.4 K in the polar strategy. This in turn drives a strong strategy dependence of the resulting stratospheric moistening, with 49% (2.2 ppm) increase in tropical lowermost stratospheric water vapour at 100 hPa in EQ compared to 14% (0.6 ppm) in POLAR. The strong increase in lower stratospheric water vapour constitutes a positive radiative forcing (here estimated at 0.15-0.54 W/m^2 depending on strategy) that offsets some of the direct aerosol-induced surface cooling from reduced insolation, thereby constituting an important contributing factor when considering the efficacy of each SAI strategy, as discussed in Zhang et al. (2023). The strong SAI strategy dependence of the lower stratospheric warming also gives rise to a strong strategy dependence of the magnitude of the SAI-induced changes in stratospheric transport, including the strengthening of the stratospheric polar vortex in both hemispheres, the deceleration of tropical upwelling and meridional velocities in the UTLS and shallow branch of the Brewer Dobson circulation, and the acceleration of the deep branch of the residual circulation.

Second, despite clear relationship between injection strategy - and thus the concentration of sulfate in the tropical lower stratosphere - and stratospheric circulation and climate on annual timescales, a more complicated picture emerges regarding SAI impacts on the modes of extratropical variability. In the NH during winter, the descent of the stratospheric westerly response down to the surface in the form of a positive phase of the North Atlantic Oscillation in sea-level pressure and a poleward shift of the eddy-driven jet in the Atlantic sector is only simulated under the two tropical injection strategies, i.e. EQ and 15N+15S. This leads to a significant warming of near-surface winter air temperatures in the northern Eurasia in these two

14

440   strategies (as well as a suggestion of a small cooling in western Europe). In contrast, 30N+30S and POLAR do not show a clear SAI-induced responses in these regions as the stratospheric westerly responses are smaller. In the Pacific sector, on the other hand, the three tropical/subtropical strategies – i.e. EQ, 15N+15S and 30N+30S – lead to a strengthening of the Aleutian low in the northern Pacific (somewhat stronger for the subtropical injections) and an equatorward eddy-driven jet shift in that region. This increases near surface air temperatures over the western US and Alaskan regions. Unlike the top-down response

445   in the Atlantic sector, the Pacific sector responses likely reflect a large scale wave response caused by tropospheric teleconnections and changes in tropical Pacific convective heating, although further work and more idealised experiments would be needed to fully diagnose the details of such teleconnections.

In the SH high latitudes, we find that both EQ and POLAR drive a positive SAM sea-level pressure response alongside a

450   poleward shift of SH eddy-driven jet. The response weakens for 15N+15S and changes signs for 30N-30S, where a small negative SAM sea-level pressure pattern and an equatorward shift of eddy-driven jet is found instead. We suggested differences in the primary driver of the responses between the annual and polar strategies, with the response in EQ, 15N+15S and 30N+30S driven primarily by the influence of lower stratospheric heating and its poleward extent, in a manner consistent with that proposed in Bednarz et al. (2022b), and the response in POLAR driven mostly by the direct radiative impact of the high latitude

455   cooling.

Third, the study finds a strong strategy dependence of the SAI-induced changes in the intensity of the tropical Hadley and Walker Circulations in the troposphere. Both EQ and 15N+15S show significant weakening of the Hadley Circulation that is not reproduced for 30N+30S and POLAR. The Walker Circulation, on the other hand, weakens under all SAI strategies, but

460   the magnitude of the changes is strongest for the tropical and subtropical injections. The stronger weakening of the Walker Circulation in these strategies coincides with near-air surface temperatures increasing preferentially over eastern Pacific resembling a canonical El Nino response; whilst the smaller response in POLAR coincides with more extensive warming over the equatorial Pacific. In general, the SAI-induced weakening of the tropical circulations result in consistent 'dry gets wetter, wet gets drier' impacts on the tropical precipitation patterns. Unlike a clear strategy dependence of the intensity of tropical

465   circulations, no clear strategy dependence is found for the position of the Hadley and Walker Circulations, with the simulated changes likely indicating imperfect compensation of the GHG-induced changes.

Finally, the results show contrasting SAI-induced ozone responses across the four strategies, and varying depending on the region. In the tropics, ozone changes are largely a function of changes in ozone transport caused by the SAI-induced modulation

470   of the Brewer Dobson Circulation. These largely cancel out when integrated over the depth of the atmosphere, with significant response found only for the EQ strategy (10 DU ozone decrease at the equator compared to the same period in SSP2-4.5). In the NH mid- and high latitudes, EQ and 15N+15S show year-round column ozone increases driven by the SAI-induced changes in BDC and the large-scale ozone transport. For 30N+30S and POLAR, on the other hand, dynamically driven ozone changes

are smaller and offset by the now larger chemical ozone losses from enhanced halogen activation on sulfate, leading to small

475 negative to zero changes in total ozone columns. In the SH, while ozone columns increase in the subtropics for EQ and 15N+15S, in the mid and high latitudes all strategies show reductions of column ozone, albeit likely brought by different processes: enhanced chemical ozone loss from halogen activation (for 30N+30S and POLAR) and/or dynamically induced ozone reductions inside the strengthened polar vortex (EQ and 15N+15S).

480 The results highlight the complex interplay of various radiative, dynamical and chemical processes driving the atmospheric response to SAI, not only on the global but in particular on regional and/or seasonal scales. Since all of these are affected differently by different location of SO_2 injection, the study demonstrates the importance the choice of the injection strategy has for the simulated climate outcomes. Given the large uncertainty in model representation of the various contributing processes, the results underscore the need for more research done in narrowing the associated uncertainties, including the

485 evaluation of the strategy dependence in a multi-model framework. An improved understanding of the role of injection strategy from this study is thus particularly relevant for designing and informing future inter-model comparisons, including the next phase of the GeoMIP project.

Acknowledgements

Authors contributions

EMB analysed the results and wrote the manuscript. YZ and EMB carried out the simulations, with assistance from DV. All authors contributed to the discussion of the results and writing of the manuscript.

Competing interests

500 The authors declare no conflict of interests.

References

Abalos, M., Calvo, N., Benito-Barca, S., Garny, H., Hardiman, S. C., Lin, P., Andrews, M. B., Butchart, N., Garcia, R., Orbe, C., Saint-Martin, D., Watanabe, S., and Yoshida, K.: The Brewer–Dobson circulation in CMIP6, Atmos. Chem. Phys., 21, 13571–13591, https://doi.org/10.5194/acp-21-13571-2021, 2021.

505

Bala, G., Duffy, P. B., and Taylor, K. E.: Impact of geoengineering schemes on the global hydrological cycle, P. Natl. Acad. Sci. USA, 105, 7664–7669, https://doi.org/10.1073/pnas.0711648105, 2008.

Banerjee, A., Butler, A. H., Polvani, L. M., Robock, A., Simpson, I. R., and Sun, L.: Robust winter warming over Eurasia

510 under stratospheric sulfate geoengineering – the role of stratospheric dynamics, Atmos. Chem. Phys., 21, 6985–6997, https://doi.org/10.5194/acp-21-6985-2021, 2021.

Bednarz, E. M., Visioni, D., Kravitz, B., Jones, A., Haywood, J. M., Richter, J., MacMartin, D. G., and Braesicke, P.: Climate response to off-equatorial stratospheric sulfur injections in three Earth system models – Part 2: Stratospheric and free-

515 tropospheric response, Atmos. Chem. Phys., 23, 687–709, https://doi.org/10.5194/acp-23-687-2023, 2023.

Bednarz, E. M., Visioni, D., Banerjee, A., Braesicke, P., Kravitz, B., MacMartin, D. G.: The overlooked role of the stratosphere under a solar constant reduction, Geophysical Research Letters, 49, e2022GL098773. https://doi.org/10.1029/2022GL098773, 2022a.

520

Bednarz, E. M., Visioni , D., Richter, J. H., Butler, A. H., MacMartin , D. G.: Impact of the latitude of stratospheric aerosol injection on the Southern Annular Mode, Geophysical Research Letters, 49, e2022GL100353. https://doi.org/10.1029/2022GL100353, 2022b.

525 Cheng, W., MacMartin, D. G., Kravitz, B., Visioni, D., Bednarz, E. M., Xu, Y., Luo, Y., Huang, L., Hu, Y., Staten, P. W., Hitchcock, P., Moore, J. C., Guo, A., Deng, X.: Changes in Hadley circulation and intertropical convergence zone under strategic stratospheric aerosol geoengineering. npj Clim Atmos Sci 5, 32. https://doi.org/10.1038/s41612-022-00254-6, 2022.

Calvo, N., Iza, M., Hurwitz, M. M., Manzini, E., Peña-Ortiz, C., Butler, A. H., Cagnazzo, C., Ineson, S., & Garfinkel, C. I.:

530 Northern Hemisphere Stratospheric Pathway of Different El Niño Flavors in Stratosphere-Resolving CMIP5 Models, Journal of Climate, 30(12), 4351-4371, 2017.

Danabasoglu, G., Lamarque, J.-F., Bacmeister, J., Bailey, D. A., DuVivier, A. K., Edwards, J., Emmons, L. K., Fasullo, J.,
Garcia, R., Gettelman, A., Hannay, C., Holland, M. M., Large, W. G., Lauritzen, P. H., Lawrence, D. M., Lenaerts, J. T. M.,
535   Lindsay, K., Lipscomb, W. H., Mills, M. J., Neale, R., Oleson, K. W., Otto-Bliesner, B., Phillips, A. S., Sacks, W., Tilmes, S.,
van Kampenhout, L., Vertenstein, M., Bertini, A., Dennis, J., Deser, C., Fischer, C., Fox-Kemper, B., Kay, J. E., Kinnison, D.,
Kushner, P. J., Larson, V. E., Long, M. C., Mickelson, S., Moore, J. K., Nienhouse, E., Polvani, L., Rasch, P. J., and Strand,
W. G.: The Community Earth System Model Version 2 (CESM2), J. Adv. Model. Earth Sy., 12, e2019MS001916,
https://doi.org/10.1029/2019MS001916, 2020.
540

Davis, N. A., Visioni, D., Garcia, R. R., Kinnison, D. E., Marsh, D. R., Mills, M. J., Richter, J. H., Tilmes, S., Bardeen, C.,
Gettelman, A., Glanville, A. A., MacMartin, D. G., Smith, A. K., and Vitt, F.: Climate, variability, and climate sensitivity of
"Middle Atmosphere" chemistry configurations of the Community Earth System Model Version 2, Whole Atmosphere
Community Climate Model Version 6 (CESM2(WACCM6)), https://doi.org/10.22541/essoar.167117634.40175082/v1, 2022.
545

England, M., L. Polvani, and L. Sun: Contrasting the Antarctic and Arctic Atmospheric Responses to Projected Sea Ice Loss
in the Late Twenty-First Century. J. Climate, 31, 6353–6370, https://doi.org/10.1175/JCLI-D-17-0666.1, 2018.

Forster P. M. de S., Shine K. P., Geophys. Res. Lett. 26, 3309, 1999.
550

Fricko, O., P. Havlik, J. Rogelj, Z. Klimont, M. Gusti, N. Johnson, P. Kolp, M. Strubegger, H. Valin, M. Amann, T. Ermolieva,
N. Forsell, M. Herrero, C. Heyes, G. Kindermann, V. Krey, D. L. McCollum, M. Obersteiner, S. Pachauri, S. Rao, E. Schmid,
W. Schoepp, K. Riahi: The marker quantification of the Shared Socioeconomic Pathway 2: A middle-of-the-road scenario for
the 21st century, Global Environmental Change, Volume 42, Pages 251-267, https://doi.org/10.1016/j.gloenvcha.2016.06.004,
555   2017.

Gettelman, A., Mills, M. J., Kinnison, D. E., Garcia, R. R., Smith, A. K., Marsh, D. R., Tilmes, S., Vitt, F., Bardeen, C. G.,
McInerny, J., Liu, H.-L., Solomon, S. C., Polvani, L. M., Emmons, L. K., Lamarque, J.-F., Richter, J. H., Glanville, A. S.,
Bacmeister, J. T., Phillips, A. S., Neale, R. B., Simpson, I. R., DuVivier, A. K., Hodzic, A., and Randel, W. J.: TheWhole
560   Atmosphere Community ClimateModel Version 6 (WACCM6), J. Geophys. Res.-Atmos., 124, 12380–12403,
https://doi.org/10.1029/2019JD030943, 2019.

Guo, A., Moore, J. C., and Ji, D.: Tropical atmospheric circulation response to the G1 sunshade geoengineering radiative
forcing experiment, Atmos. Chem. Phys., 18, 8689–8706, https://doi.org/10.5194/acp-18-8689-2018, 2018.
565

Haywood, J. M., Jones, A., Bellouin, N., and Stephenson, D.: Asymmetric forcing from stratospheric aerosols impacts Sahelian rainfall, Nat. Clim. Change, 3, 660–665, 2013.

Jones, A., Haywood, J. M., Scaife, A. A., Boucher, O., Henry, M., Kravitz, B., Lurton, T., Nabat, P., Niemeier, U., Séférian,
570   R., Tilmes, S., and Visioni, D.: The impact of stratospheric aerosol intervention on the North Atlantic and Quasi-Biennial Oscillations in the Geoengineering Model Intercomparison Project (GeoMIP) G6sulfur experiment, Atmos. Chem. Phys., 22, 2999–3016, https://doi.org/10.5194/acp-22-2999-2022, 2022.

Kang, S.M., Xie, S.P., Shin, Y., Kim, H., Hwang, Y.T., Stuecker, M.F., Xiang, B. and Hawcroft, M.,: Walker circulation
575   response to extratropical radiative forcing. Science Advances, 6(47), eabd3021, https://doi.org/10.1126/sciadv.abd3021, 2020.

Kravitz, B., MacMartin, D.G: Uncertainty and the basis for confidence in solar geoengineering research. Nat Rev Earth Environ 1, 64–75, 2020.

580   Kravitz, B., Robock, A., Tilmes, S., Boucher, O., English, J. M., Irvine, P. J., Jones, A., Lawrence, M. G., MacCracken, M., Muri, H., Moore, J. C., Niemeier, U., Phipps, S. J., Sillmann, J., Storelvmo, T., Wang, H., and Watanabe, S.: The Geoengineering Model Intercomparison Project Phase 6 (GeoMIP6): simulation design and preliminary results, Geosci. Model Dev., 8, 3379–3392, https://doi.org/10.5194/gmd-8-3379-2015, 2015.

585   Krishnamohan, K.-P. S.-P., Bala, G., Cao, L., Duan, L., and Caldeira, K.: Climate system response to stratospheric sulfate aerosols: sensitivity to altitude of aerosol layer, Earth Syst. Dynam., 10, 885–900, https://doi.org/10.5194/esd-10-885-2019, 2019.

Lee, W. R., MacMartin, D. G., Visioni, D., Kravitz, B., Chen, Y., Moore, J. C., et al.: . High-latitude stratospheric aerosol
590   injection to preserve the Arctic. Earth's Future, 11, e2022EF003052. https://doi.org/10.1029/2022EF003052, 2023.

Lee, Walker R., D. G. MacMartin, D. Visioni, B. Kravitz: High-latitude stratospheric aerosol geoengineering can be more effective if injection is limited to spring, Geophysical Research Letters, 48, e2021GL092696, doi: 10.1029/2021GL092696, 2021.

595

Liu, X., Ma, P.-L., Wang, H., Tilmes, S., Singh, B., Easter, R. C., Ghan, S. J., and Rasch, P. J.: Description and evaluation of a new four-mode version of the Modal Aerosol Module (MAM4) within version 5.3 of the Community Atmosphere Model, Geosci. Model Dev., 9, 505–522, https://doi.org/10.5194/gmd-9-505-2016, 2016.

600 MacMartin, D. G., Visioni, D., Kravitz, B., Richter, J., Felgenhauer, T., Lee, W. R., Morrow, D. R., Parson, E. A., Sugiyama, M.:. Scenarios for modeling solar radiation modification. Proceedings of the National Academy of Sciences, 119(33). https://doi.org/10.1073/pnas.2202230119, 2022.

Meinshausen, M., Nicholls, Z. R. J., Lewis, J., Gidden, M. J., Vogel, E., Freund, M., Beyerle, U., Gessner, C., Nauels, A.,
605 Bauer, N., Canadell, J. G., Daniel, J. S., John, A., Krummel, P. B., Luderer, G., Meinshausen, N., Montzka, S. A., Rayner, P. J., Reimann, S., Smith, S. J., van den Berg, M., Velders, G. J. M., Vollmer, M. K., and Wang, R. H. J.: The shared socio-economic pathway (SSP) greenhouse gas concentrations and their extensions to 2500, Geosci. Model Dev., 13, 3571–3605, https://doi.org/10.5194/gmd-13-3571-2020, 2020.

610 Niemeier, U., Schmidt, H., Alterskjær, K., and Kristjánsson, J. E.: Solar irradiance reduction via climate engineering: Impact of different techniques on the energy balance and the hydrological cycle, J. Geophys. Res. Atmos., 118, 11,905– 11,917, doi:10.1002/2013JD020445, 2013.

Richter, J. H., Visioni, D., MacMartin, D. G., Bailey, D. A., Rosenbloom, N., Dobbins, B., Lee, W. R., Tye, M., and Lamarque,
615 J.-F.: Assessing Responses and Impacts of Solar climate intervention on the Earth system with stratospheric aerosol injection (ARISE-SAI): protocol and initial results from the first simulations, Geosci. Model Dev., 15, 8221–8243, https://doi.org/10.5194/gmd-15-8221-2022, 2022.

Richter, J. H., Tilmes, S., Mills, M. J., Tribbia, J. J., Kravitz, B., Macmartin, D. G., Vitt, F., and Lamarque, J. F.: Stratospheric
620 dynamical response and ozone feedbacks in the presence of $SO2$ injections, J. Geophys. Res.-Atmos., 122, 12557–12573, https://doi.org/10.1002/2017JD026912, 2017.

Scinocca, J. F., Reader, M. C., Plummer, D. A., Sigmond, M., Kushner, P. J., Shepherd, T. G., and Ravishankara, A. R.: Impact of sudden Arctic sea-ice loss on stratospheric polar ozone recovery, Geophys. Res. Lett., 36, L24701,
625 doi:10.1029/2009GL041239, 2009.

Simpson, I., Tilmes, S., Richter, J., Kravitz, B., MacMartin, D., Mills, M., Fasullo, J. T., and Pendergrass, A. G.: The regional hydroclimate response to stratospheric sulfate geoengineering and the role of stratospheric heating, J. Geophys. Res.-Atmos., 124, 12587–12616, https://doi.org/10.1029/2019JD031093, 2019.
630
Solomon, S., K. H. Rosenlof, R. W. Portmann, J. S. Daniel, S. M. Davis, T. J. Sanford, G.-K. Plattner, Contributions of stratospheric water vapor to decadal changes in the rate of global warming. Science 327, 1219–1223, 2010.

635   Sun, L., C. Deser, L. Polvani, and R. Tomas: Influence of projected Arctic sea ice loss on polar stratospheric ozone and circulation in spring. Environ. Res. Lett., 9, 084016, https://doi.org/10.1088/1748-9326/9/8/084016, 2014.

Thompson, D. W. J., Wallace, J. M.,Hegerl, G. C.: Annular Modes in the Extratropical Circulation. Part II: Trends, Journal of Climate, 13(5), 1018-1036, 2000.

640   Thompson, D. W. J., & Wallace, J. M.: Annular modes in the extratropical circulation. Part I: Month-to-Month variability. Journal of Climate, 13(5), 1000– 1016, 2000.

Thompson, D. W. J., & Wallace, J. M.: The Arctic oscillation signature in the wintertime geopotential height and temperature fields. Geophysical Research Letters, 25(9), 1297– 1300. https://doi.org/10.1029/98GL00950, 1998.

645

Tilmes, S., Richter, J. H., Kravitz, B., MacMartin, D. G., Mills, M. J., Simpson, I. R., Glanville, A. S., Fasullo, J. T., Phillips, A. S., Lamarque, J.-F., Tribbia, J., Edwards, J., Mickelson, S., and Ghosh, S.: CESM1(WACCM) Stratospheric Aerosol Geoengineering Large Ensemble Project, B. Am. Meteorol. Soc., 99, 2361–2371, https://doi.org/10.1175/BAMS-D-17-0267.1, 2018b.

650

Tilmes, S., Richter, J. H., Mills, M. J., Kravitz, B., Mac- Martin, D. G., Garcia, R. R., Kinnison, D. E., Lamarque, 60 J. F., Tribbia, J., and Vitt, F.: Effects of different stratospheric SO2 injection altitudes on stratospheric chemistry and dynamics, J. Geophys. Res.-Atmos., 123, 4654–4673, https://doi.org/10.1002/2017JD028146, 2018a.

655   Tilmes, S., Richter, J. H., Kravitz, B., MacMartin, D. G., Glanville, A. S., Visioni, D., Kinnison, D. E., and Müller, R.: Sensitivity of total column ozone to stratospheric sulfur injection strategies, Geophys. Res. Lett., 48, e2021GL094058, https://doi.org/10.1029/2021GL094058, 2021.

Tilmes, S., Visioni, D., Jones, A., Haywood, J., Séférian, R., Nabat, P., Boucher, O., Bednarz, E. M., and Niemeier, U.:
660   Stratospheric ozone response to sulfate aerosol and solar dimming climate interventions based on the G6 Geoengineering Model Intercomparison Project (GeoMIP) simulations, Atmos. Chem. Phys., 22, 4557–4579, https://doi.org/10.5194/acp-22-4557-2022, 2022.

Pitari, G., Aquila, V., Kravitz, B., Robock, A., Watanabe, S., Cionni, I., Luca, N. D., Genova, G. D., Mancini, E., and Tilmes,
665   S.: Stratospheric ozone response to sulfate geoengineering: Results from the Geoengineering Model Intercomparison Project (GeoMIP), J. Geophys. Res.-Atmos., 119, 2629–2653, https://doi.org/10.1002/2013JD020566, 2014.

21

Riese, M., Ploeger, F., Rap, A., Vogel, B., Konopka, P., Dameris, M., and Forster, P.: Impact of uncertainties in atmospheric mixing on simulated UTLS composition and related radiative effects, J. Geophys. Res., 117, D16305, doi:10.1029/2012JD017751, 2012.

Ring, M. J., and Plumb, R. A.: Forced Annular Mode Patterns in a Simple Atmospheric General Circulation Model, Journal of the Atmospheric Sciences, 64(10), 3611-3626, 2007.

Yeh, S.-W., J.-S. Kug, B. Dewitte, M.-H. Kwon, B. P. Kirtman, and F.-F. Jin: El Niño in a changing climate. Nature, 461, 511–514, doi:10.1038/nature08316, 2009.

Visioni, D., Bednarz, E. M., Lee, W. R., Kravitz, B., Jones, A., Haywood, J. M., and MacMartin, D. G.: Climate response to off-equatorial stratospheric sulfur injections in three Earth system models – Part 1: Experimental protocols and surface changes, Atmos. Chem. Phys., 23, 663–685, https://doi.org/10.5194/acp-23-663-2023, 2023.

Visioni, D., Tilmes, S., Bardeen, C., Mills, M., MacMartin, D. G., Kravitz, B., and Richter, J. H.: Limitations of assuming internal mixing between different aerosol species: a case study with sulfate geoengineering simulations, Atmos. Chem. Phys., 22, 1739–1756, https://doi.org/10.5194/acp-22-1739-2022, 2022.

Visioni, D., MacMartin, D. G., & Kravitz, B.: Is turning down the sun a good proxy for stratospheric sulfate geoengineering? Journal of Geophysical Research: Atmospheres, 126, e2020JD033952. https://doi.org/10.1029/2020JD033952, 2021a.

Visioni, D., MacMartin, D. G., Kravitz, B., Boucher, O., Jones, A., Lurton, T., Martine, M., Mills, M. J., Nabat, P., Niemeier, U., Séférian, R., and Tilmes, S.: Identifying the sources of uncertainty in climate model simulations of solar radiation modification with the G6sulfur and G6solar Geoengineering Model Intercomparison Project (GeoMIP) simulations, Atmos. Chem. Phys., 21, 10029-10063, 2021b.

Visioni, D., MacMartin, D. G., Kravitz, B., Lee, W., Simpson, I. R., & Richter, J. H.: Reduced poleward transport due to stratospheric heating under stratospheric aerosols geoengineering. Geophysical Research Letters, 47, e2020GL089470. https://doi.org/10.1029/2020GL089470, 2020.

World Meteorological Organization (WMO), Scientific Assessment of Ozone Depletion: 2022, GAW Report No. 278, 509 pp., WMO, Geneva, 2022.
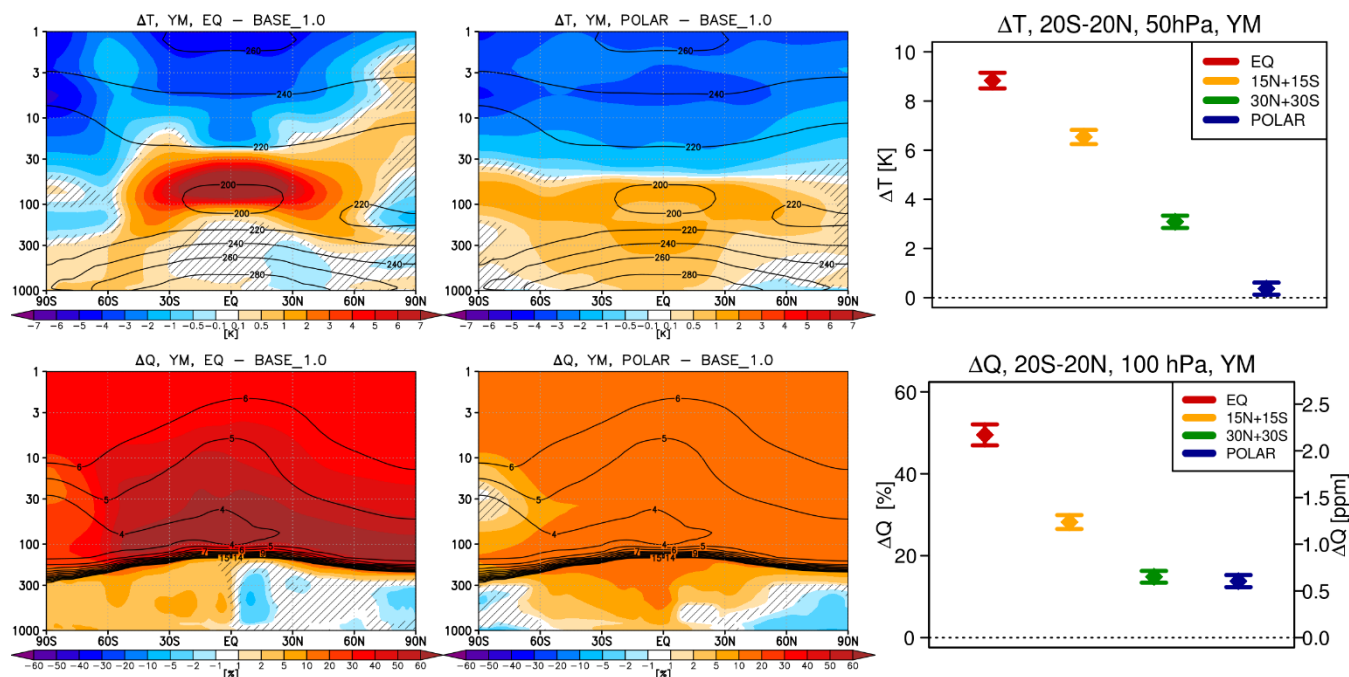
Zhang, Y., MacMartin, D. G., Visioni, D., Bednarz, E., and Kravitz, B.: Introducing a Comprehensive Set of Stratospheric Aerosol Injection Strategies, EGUsphere [preprint], https://doi.org/10.5194/egusphere-2023-117, 2023.
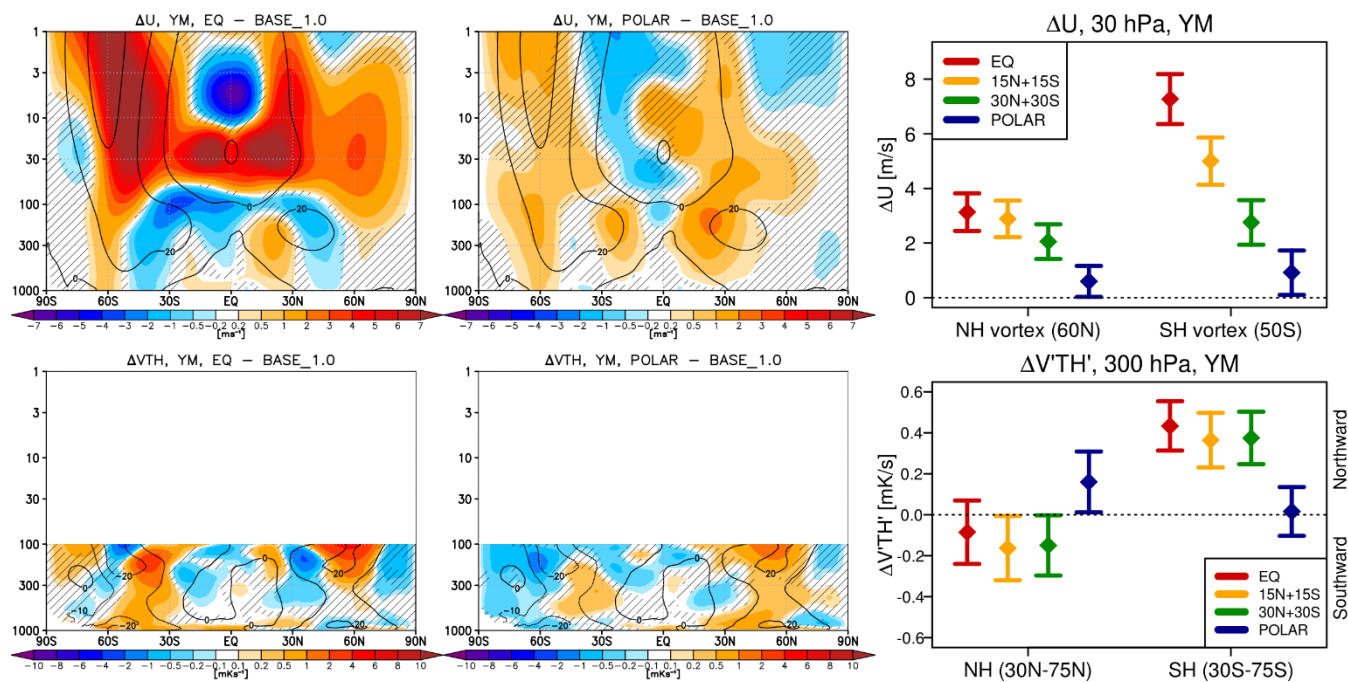
Figure 1. Shading (left and middle): yearly mean changes in (top) temperatures and (bottom) water vapour for (left) EQ and (middle) POLAR strategy compared to the baseline period (2008-2027). Contours show the corresponding values in the baseline period for refence (in units of K and ppm for temperature and water vapour respectively). Hatching indicate regions where the response is not statistically significant, taken as smaller than ±2 standard errors of the difference in means. See Fig. S2 in Supplementary Material for the analogous changes in the 15N+15S and 30N+30S strategies. Right columns show the changes in the tropical (20°S-20°N) temperatures at 50 hPa and water vapour at 100 hPa in each of the four strategies. The errorbars denote ±2 standard error of the difference in means.

Figure 2. Shading (left and middle): yearly mean changes in (top) zonal winds and (bottom) northward meridional eddy heat flux below 100 hPa for (left) EQ and (middle) POLAR strategy compared to the baseline period. Contours show the corresponding values in the baseline period for refence. See Fig. S3 in Supplementary Material for the analogous changes in the 15N+15S and 30N+30S strategies. Right column shows the changes in (top) the strength of the NH (60°S) and SH (50°S) polar vortex at 30 hPa and (b) northward meridional heat flux at 300 hPa averaged over the NH (30°N-75°N) and SH (30°S-75°S) extra-tropics for each of the four strategies compared to the baseline period. Hatching in (left-middle) and errorbars in (right) as in Fig. 1.
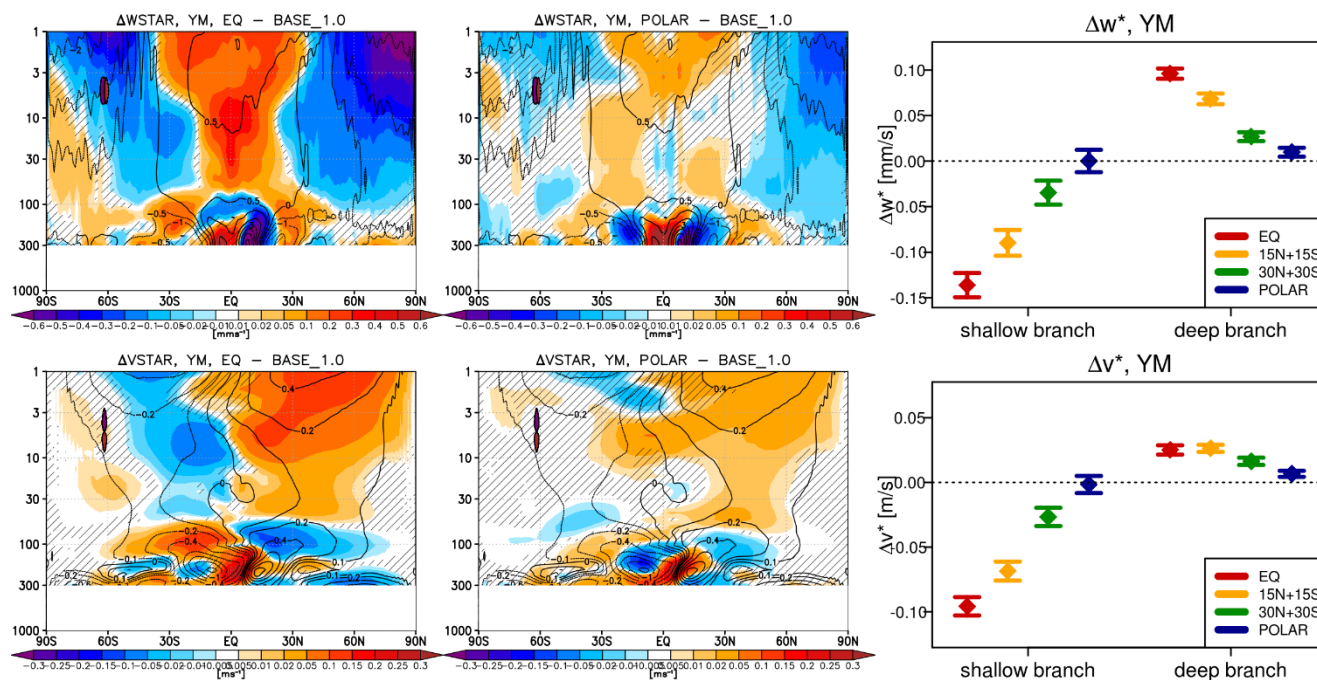
Figure 3. Shading (left and middle): yearly mean changes in residual (top) vertical and (bottom) meridional velocities for (left) EQ and (middle) POLAR strategy compared to the baseline period. Contours show the corresponding values in the baseline period for refence. See Fig. S6 in Supplementary Material for the analogous changes in the 15N+15S and 30N+30S strategies. Right column shows the changes in the shallow and deep branches of BDC; these are defined as means over 15°S-15°N at 100 hPa and over 25°S-25°N at 30 hPa, respectively, for w* and as difference between 0°-90°N and 90°S-0° at 70 hPa and at 30 hPa, respectively, for v*. Hatching in (left-middle) and errorbars in (right) as in Fig. 1.
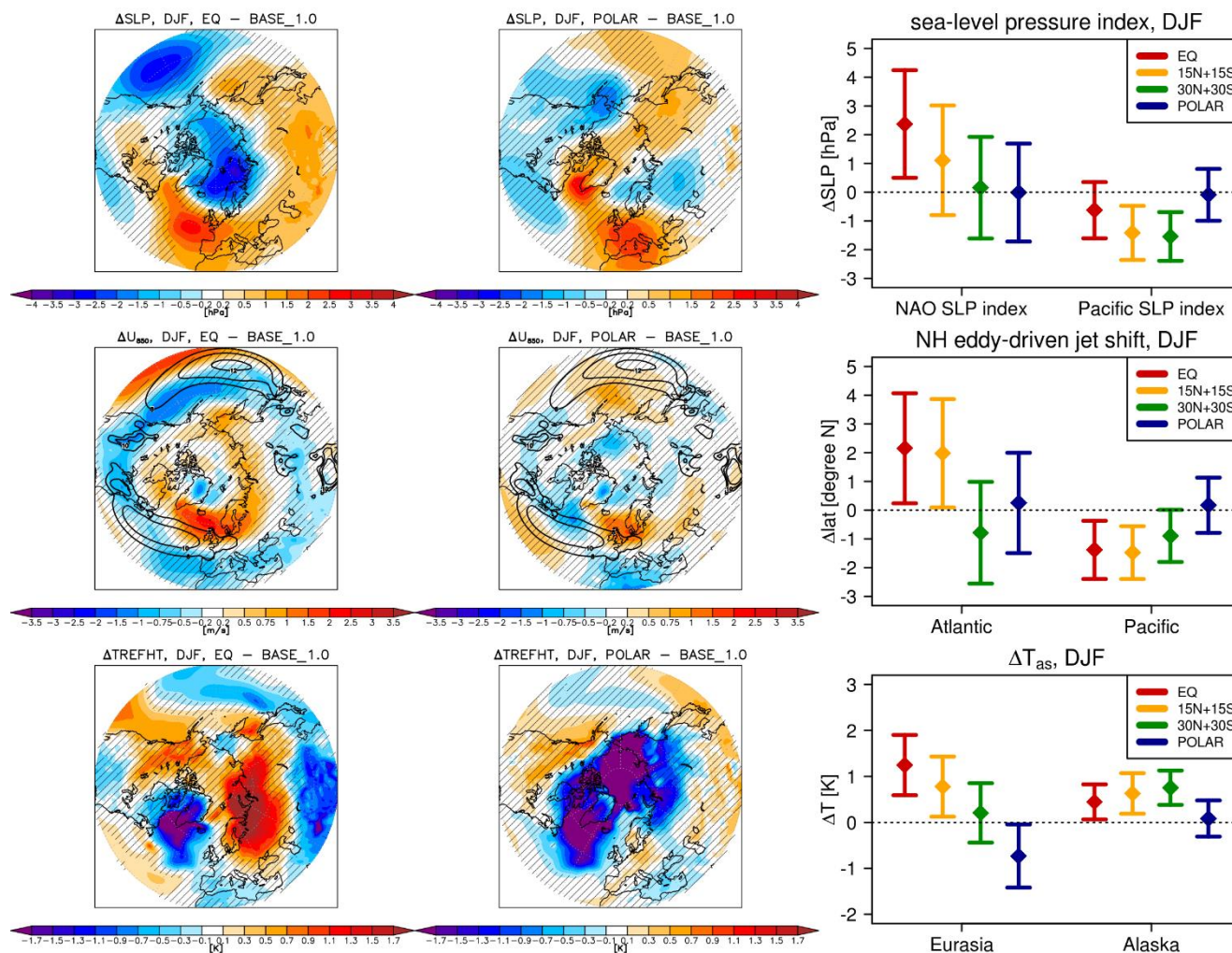
Figure 4. Shading (left and middle): DJF mean changes in (top) sea level pressure, (middle) zonal wind at 850 hPa, and (bottom) near-surface atmospheric temperatures northward from 30°N for (left) EQ and (middle) POLAR strategy compared to the baseline period. Contours in (middle) show the corresponding values in the baseline period for refence and denote the position of the climatological jet. See Fig. S7 in Supplementary Material for the analogous changes in the 15N+15S and 30N+30S strategies. Right columns show changes in the NAO and Pacific sea-level pressure index, position of the Atlantic and Pacific eddy-driven jet, and temperatures over Eurasian and Alaska regions (see text for details). Hatching in (left-middle) and errorbars in (right) as in Fig. 1.
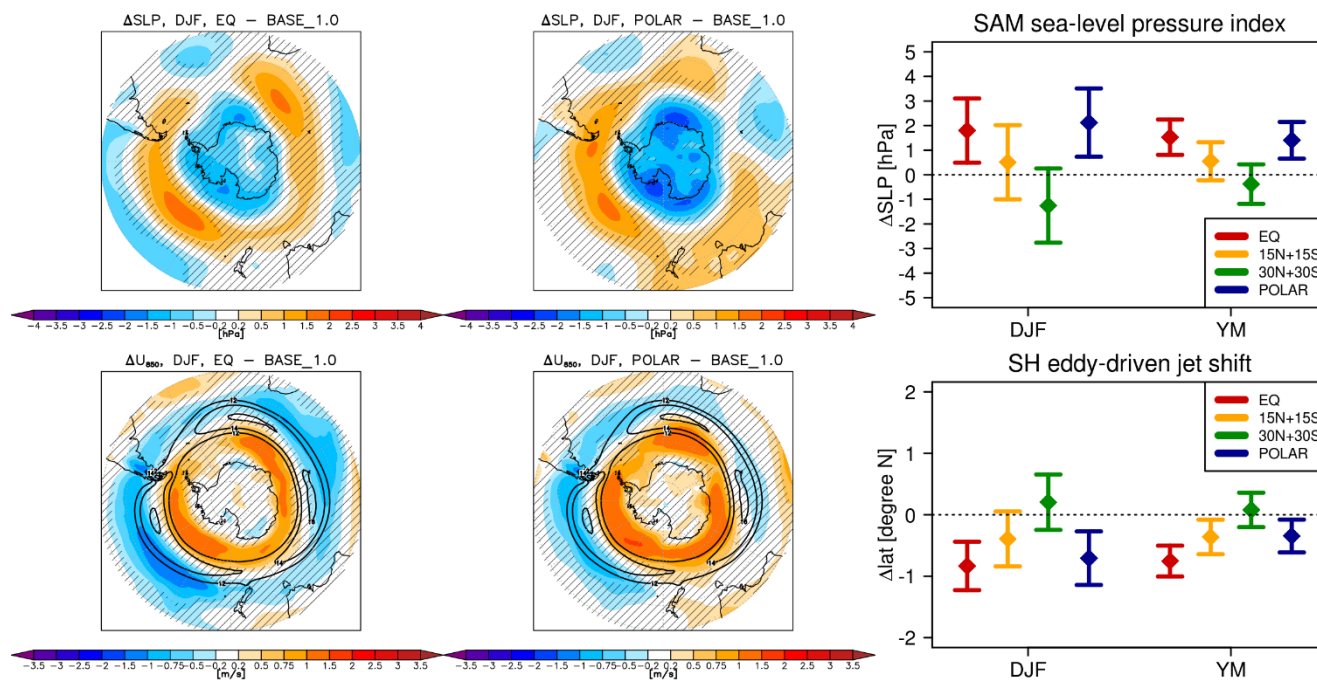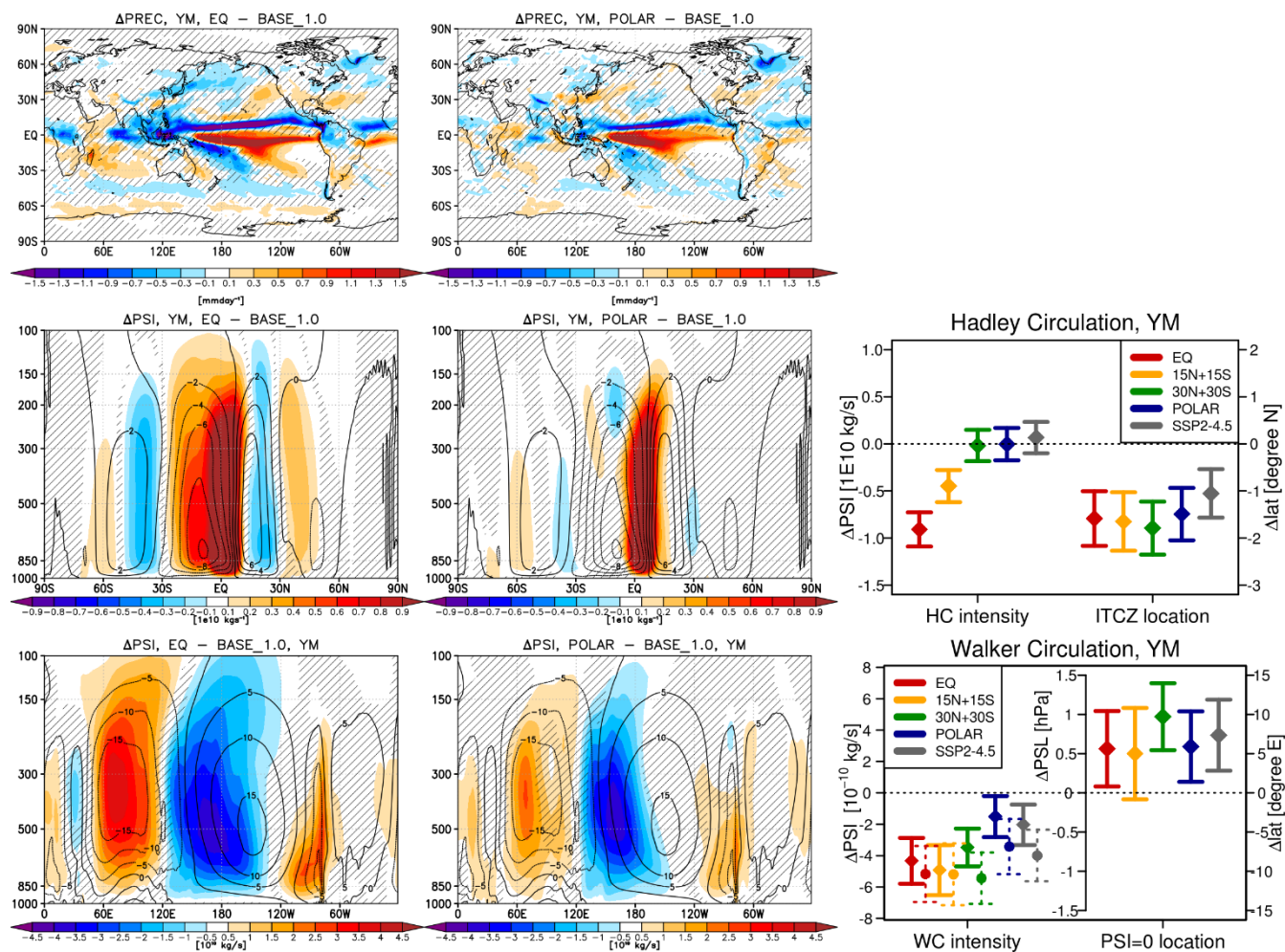
Figure 5. Shading (left and middle): DJF mean changes in (top) sea level pressure, and (bottom) zonal wind at 850 hPa southward from 30°S for (left) EQ and (middle) POLAR strategy compared to the baseline period. Contours in (middle) show the corresponding values in the baseline period for refence and denote the position of the climatological jet. See Fig. S10 in Supplementary Material for the analogous changes in the 15N+15S and 30N+30S strategies. Right columns show changes in SAM sea level pressure index and the position of SH eddy-driven jet (see text for details). Hatching in (left-middle) and errorbars in (right) as in Fig. 1.
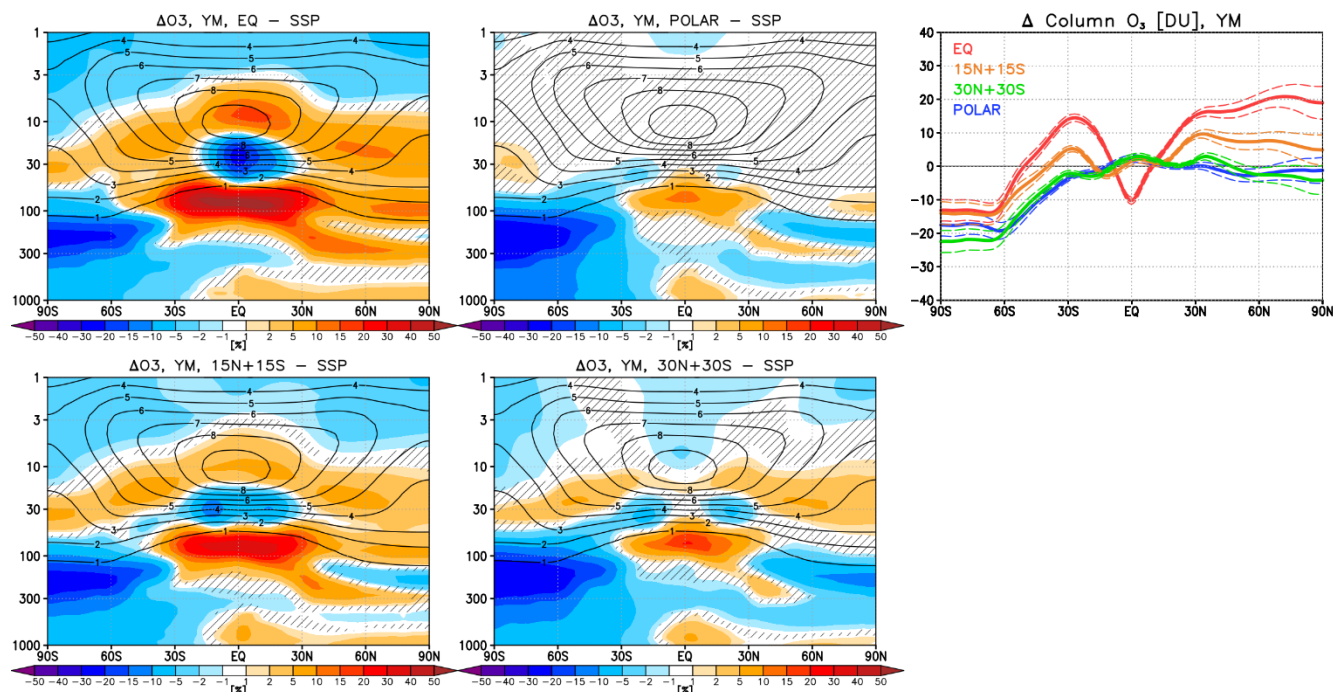
Figure 6. Shading (left and middle): Yearly mean changes in (top) precipitation, (middle) meridional mass stream function, and (bottom) zonal mass stream function for (left) EQ and (middle) POLAR strategy compared to the baseline period. Contours in middle and bottom show the corresponding values in the baseline period for refence. See Fig. S11 in Supplementary Material for the analogous changes in the 15N+15S and 30N+30S strategies. Right column shows changes in the intensity of Hadley Circulation and the position of ITCZ, and in the intensity of Walker Circulation (diamond and solid lines show the results derived using the stream function method, point and dashed lines show the results derived using the sea-level pressure method) and the position of the transition between its Pacific and Indian Ocean cells for each of the four SAI strategies as well as the control SSP2-4.5 simulation (see text for details). Hatching in (left-middle) and errorbars in (right) as in Fig. 1.
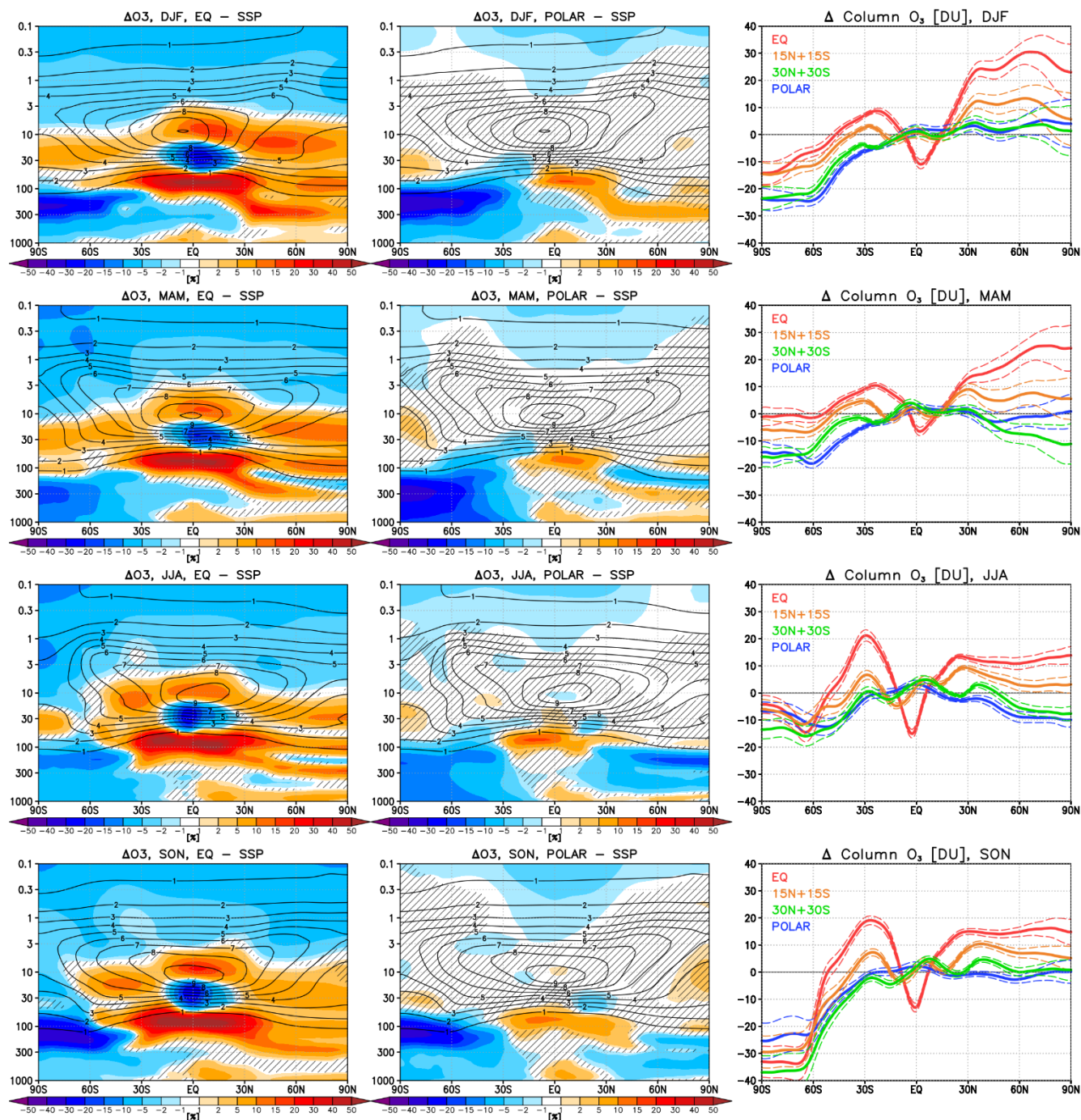
Figure 7. Shading (left and middle): Yearly mean changes in ozone mixing ratios for each of the EQ, 15N+15S, 30N+30S and POLAR strategies compared to the same period (i.e. 2050-2069) of the control SSP2-4.5 simulation. Contours show the corresponding values in SSP2-4.5 for refence (in the units of ppm). Hatching as in Fig. 1. Right: Yearly mean changes in total column ozone for each of the four strategies as a function of latitude. Dashed lines indicate the associates ±2 standard errors of the difference in means.

Figure 8. Shading (left and middle): Seasonal mean (top to bottom: DJF, MAM, JJA and SON) changes in ozone mixing ratios for the (left) EQ and (middle) POLAR strategies compared to the same period (i.e. 2050-2069) of the control SSP2-4.5 simulation. Contours show the corresponding values in SSP2-4.5 for refence (in the units of ppm). Hatching as in Fig. 1. See Fig. S13 in Supplementary Material for the analogous changes in the 15N+15S and 30N+30S strategies. Right: Seasonal mean changes in total

775

column ozone for each of the four strategies as a function of latitude. Dashed lines indicate the associated ±2 standard errors of the difference in means.